Spatial Uniformity of Atmospheric Pressure Discharges: A Simulation Study

M. M. Iqbal[1] and M. M. Turner[1]

[1]School of Physical Sciences and National Centre for Plasma Science and Technology, Dublin City University, Dublin 9, Ireland

Spatial uniformity is important in most applications of dielectric barrier discharges operating at atmospheric pressure. However, such uniformity is not easily achieved. Under many conditions, a filamentary structure usually develops. In this paper, we employ a two-dimensional self-consistent fluid model to explore the influence of several factors on the evolution of spatial structure of dielectric barrier discharges. In particular, we contrast the behaviour of discharges in pure helium and He-N$_2$ gas mixture, which represent the reduction in breakdown voltage of gas during the evolvement of uniform glow discharge plasma. The transformation from filamentary to uniform mode of discharge plasma is analyzed by the phenomenon of coalescence of filaments and we investigate the effect of several external discharge parameters, such as driving frequency and effect of overvoltage, and the dielectric constant of the barrier material for the uniform and filamentary discharge plasmas. This simulation study is useful to describe the spatio-temporal profiles of electrons density in different phases of the filamentary, uniform Townsend and glow discharge regimes under various constraints.

1. Introduction

In recent years, dielectric barrier discharges (DBD) have emerged as one of the most exciting and interesting topics in the physics of plasma discharges at atmospheric pressure. Such discharges can be utilized in many industrial applications without the complication of vacuum systems. In DBDs, dielectric barrier layers attached to the electrodes form capacitances in series with the external circuit. The discharge is self-extinguishing, because a flow of current causes an accumulation of surface charges on the barriers during a pulse, which steadily reduces the electric field strength in the reactor gap. DBDs are therefore necessarily pulsed, or excited by oscillating voltages. Initially, an ionization avalanche is formed in the gap by the application of a voltage, and a huge number of electrons and ions are created by collisional processes, like excitation and ionization. Breakdown of dielectric barrier is more easily achieved in the presence of rare gases such as helium, neon and argon than in air at atmospheric pressure. However, applications generally require some mixture of gases, including some reactive species, and the breakdown then acts as a trigger to initiate intense chemical activity among the discharge species. The instant beginning of this chemical activity is essential to most applications for the development of uniform channel of ionized gas. The magnitude of the breakdown voltage can be determined approximately by the Paschen curve [1] for a particular gas, or mixture of gases, i.e., pd^1 versus breakdown voltage (V_b). The charged particle density grows rapidly after breakdown is initiated, and ultimately forms a discharge plasma near the cathodic barrier due to intense ionization in this region. A very important effect of dielectric barriers with a permittivity greater than one in the presence of rare gases is to reduce the breakdown voltage below that of air at atmospheric pressure. Moreover, the formation of uniform discharge plasmas can be achieved by the adjustment of external

---

[1]   *pd*: pressure×gap distance

operating discharge parameters, such as overvoltage (usually defined as the difference between the external applied voltage and breakdown voltage), driving frequency, gap distance between the barriers, dielectric barrier thickness and variable amount of N_2 impurities. Keeping all these characteristics in focus, it is possible to control the dynamic behaviour of the dielectric barrier discharges for different types of applications.

Several scientific groups are trying to establish techniques for the reliable and efficient use of DBDs in applications, such as surface modification and etching, deposition of thin films, pollution control, ozone generation, the sterilization of biological samples, aerospace and aerodynamics applications [2 - 8]. In the field of non-thermal discharge plasmas, the evolution of various kinds of non-uniformities still requires attention, in order to achieve a full understanding of the complex mechanisms. Massines and her co-workers [9] performed an experimental study of DBD at a particular frequency and compared the experimental results with a simple fluid model without considering the chemistry of operating helium gas. They explored the behaviour of electrons and atomic helium ions, which are responsible for the major dynamical changes in the structures of atmospheric pressure discharge during the evolution of different phases of a cycle. Kortshagen, et al. [10] worked in the similar direction at 10 kHz for the mixture of He-N_2 gas in the presence of 100 ppm N_2 impurities. They discussed the effects of dielectric barrier thickness under fixed operating input parameters and compared the experimental results with one-dimensional fluid model. The computational analysis of DBD is further expanded by the group of Golubovskii [11], which highlighted the difference between the homogeneous uniform glow and Townsend discharge modes at variable gap widths. They further analysed the effect of amplitude of external applied voltage on the development of current peaks, which are discussed with the modelling and analytical explanation for the uniform homogeneous glow and Townsend discharge modes.

In most applications, a spatially uniform glow discharge is desirable, but not easily achieved at atmospheric pressure. The normal mode of atmospheric pressure discharges is filamentary, but this can be transformed into a uniform discharge by careful control of external operating parameters. To achieve this goal, discharge modelling is important, because two-dimensional models with a detailed chemistry can accurately predict a number of features of experimental discharge plasmas. The following phases describe the time evolution of a typical discharge: i) pre-breakdown ii) breakdown phase iii) uniform glow and filamentary discharge plasma iv) decay [12, 13]. However, a special concern is to understand the occurrence of uniform and filamentary modes of DBD in a broad range of operating conditions. The bulk of recent literature in the atmospheric pressure discharges deals with a fixed frequency, i.e., 10 kHz, and explores the influence of various other external discharge variables [6, 9, 10, 11, 13, 26, 29]. The objective of the present study is to examine discharge characteristics for a wider range of source driving frequencies. The fluid model provides a complete description of the discharge plasma at much smaller computational cost than numerical solutions of the Boltzmann equation. Helium gas is the preferred medium for atmospheric pressure discharges because of features such as higher heat conductivity and rapid ionization rate from the multiple sources at lower E/P^2 and lower breakdown voltage than other gases. Our numerical simulation results do not contradict the results of earlier simulation work, but do explore a far wider range of external operating variables and constraints.

In the present paper, a two-dimensional fluid model is applied to investigate the

---

[2]   E/P: Electric field/pressure

formation of uniform and filamentary discharge modes in DBD. We discuss the characteristics of homogeneous uniform atmospheric pressure discharges in pure helium gas and the benchmarks for the uniform discharge plasma are described with the identification of four distinct spatial regions, such as cathode fall layer, negative glow, Faradays dark space and positive column. We observe that the magnitude of applied voltage is higher in pure helium than the Penning mixture of He-N_2 gas for the development of uniform glow discharge plasma. The emergence of distinct filamentary structures in different phases of a pulse are demonstrated by the application of various operating conditions, such as overvoltage and compulsive significance of higher recombination coefficient of N_2^+ ions. Coalescence of filaments in the breakdown phase occurs with an increase in frequency. The spatio-temporal characteristics of uniform atmospheric pressure discharge are investigated for a broad range of driving frequencies and relative permittivities of dielectric barrier. These results will be discussed in detail in different sections of this paper: section 2 discusses the formulation of two-dimensional fluid model in Cartesian geometry with boundary conditions, section 3 deals with simulation results in pure helium gas, section 4 distinguishes the uniform and filamentary discharge plasma in He-N_2 gas mixture, sections 5, 6 and 7 describe the spatio-temporal evolution of DBDs and finally section 8 provides the conclusions of this work.

2. Formulation of fluid model equations and chemical reaction processes

In this numerical study, a two-dimensional self-consistent fluid model is formulated such that a parallel plate dielectric barrier discharge configuration is described in the x-y Cartesian plane, with the electric field predominantly in the y direction. The flat electrodes are covered by dielectric barriers with thickness 0.1 cm and length 2.0 cm. There is a gap of 0.5 cm between the dielectric barriers. After the gas breakdown, the ignition of discharge is intensely amplified in the open rectangular area between the dielectric barriers, in the presence of pure helium and different He-N_2 gas mixtures, as shown in figure 1.
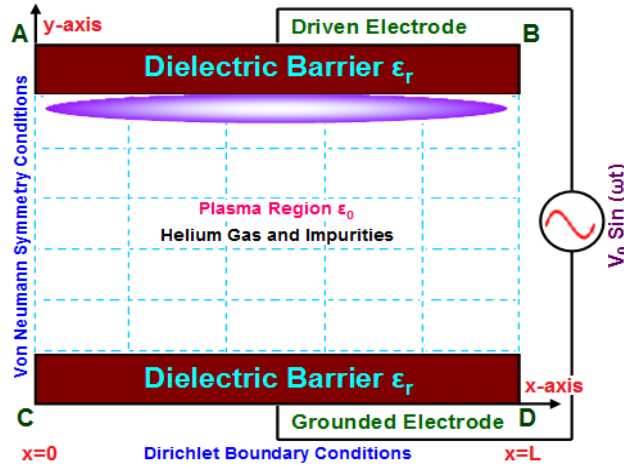

FIG. 1. Cartesian spatial mesh in the parallel plate dielectric barrier discharge configuration in the x-y plane.

The fluid model is composed of the following species: electrons, atomic and molecular ions (He^+ and He_2^+), helium metastables and excimers (He^* and He_2^*) and molecular nitrogen ions (N_2^+). The helium excited states (2^3S and 2^1S) are grouped into single state denoted by He^* and the excimers $He_2(a^3\textstyle\sum_u^+)$ are represented as

He$_2^*$. The present model is based on the coupled set of continuity equations for the plasma particle species, an electron energy density equation, and Poisson's equation for the evaluation of electric field. The drift-diffusion approximation is used in the continuity equations and electron energy density equation. Poisson's equation is solved by successive over relaxation method, and the continuity and electron energy density equations are numerically solved by using the modified strongly implicit procedure, and the entire approach is termed as a semi-implicit sequential iterative scheme [24] for the numerical solution of fluid model partial differential equations. The continuity equation for each discharge species can be written as

$$\frac{\partial n_p(x,y,t)}{\partial t} + \frac{\partial \Phi_{p_x}(x,y,t)}{\partial x} + \frac{\partial \Phi_{p_y}(x,y,t)}{\partial y} = G_p - L_p$$

(2.1)

where t stands for the time of advancement in simulation process, n_p represents the particle species number density, $\Phi_{p_x}(x,y,t)$ and $\Phi_{p_y}(x,y,t)$ are fluxes in the x and y directions. G_p and L_p represent the generation and destruction of discharge particles in the gas mixture by collision processes, which are calculated using the rates of the relevant chemical reactions. The index p distinguishes the various species. The discharge species flux is calculated by the drift-diffusion approximation as

$$\Phi_{p_x}(x,y,t) = \text{sgn}(q_p)\mu_p E_x n_p(x,y,t) - D_p\left(\frac{\partial n_p(x,y,t)}{\partial x}\right) \qquad \text{similarly} \qquad \text{for}$$

$\Phi_{p_y}(x,y,t)$. In these expressions E_x is the electric field strength in the x direction and similarly, E_y in the y direction, q_p is the particle charge, μ_p is the mobility and D_p is the diffusion coefficient.

The electron mean energy is evaluated by using the electron energy density balance equation as

$$\frac{\partial n_\varepsilon(x,y,t)}{\partial t} + \frac{\partial \Phi_{\varepsilon_x}(x,y,t)}{\partial x} + \frac{\partial \Phi_{\varepsilon_y}(x,y,t)}{\partial y} = S_\varepsilon \qquad (2.2)$$

In this equation, n_ε is the electron energy density, written as

$$n_\varepsilon(x,y,t) = n_e(x,y,t)\,\overline{\varepsilon}(x,y,t)$$

(2.3)

where $\overline{\varepsilon}$ is the electron mean energy and $n_e(x,y,t)$ is the electron density. The electron energy density flux can be expressed as

$$\Phi_{\varepsilon_x}(x,y,t) = -\frac{5}{3}\mu_e E_x n_\varepsilon(x,y,t) - \frac{5}{3}D_e\left(\frac{\partial n_\varepsilon(x,y,t)}{\partial x}\right)$$

(2.4) with a similar expression for $\Phi_{\varepsilon_y}(x,y,t)$ in the y direction. The source term for the electron energy density is composed of the following terms as

$$S_\varepsilon = -\Phi_\varepsilon(x,y,t).E(x,y,t) - n_e(x,y,t)\sum_k \overline{\varepsilon}_k k_k n_k(x,y,t)$$

where $-\Phi_\varepsilon(x,y,t).E(x,y,t)$ is the Joule heating created by the electric field and $n_e(x,y,t)\sum_k \overline{\varepsilon}_k k_k n_k(x,y,t)$ is the electron energy losses due to the elastic and inelastic collisions, respectively. The summation in the last term is only over the electron impact reactions, with n_r the density of the target particles and $\overline{\varepsilon}_k$ the threshold mean energy for the particular process.

The Poisson's equation for the electric field is represented in two-dimensions as

$$\frac{\partial(\varepsilon_r E_x)}{\partial x} + \frac{\partial(\varepsilon_r E_y)}{\partial y} = -\sum_p q_p n_p \qquad (2.5)$$

where ε_r is the relative permittivity and $q_p n_p$ represents the space charge density. The radial (E_x) and axial (E_y) field strengths are calculated from the change in the electric potential along x and y directions as $E_x = -\frac{\partial V(x,y,t)}{\partial x}$, $E_y = -\frac{\partial V(x,y,t)}{\partial y}$

2.1. Boundary conditions

The boundary conditions for the rectangular integration domain are shown in figure 1. A set of von Neumann symmetry boundary conditions is imposed on the virtual boundaries, i.e., AC and BD. Therefore, the discharge species density, electron energy density and electrical potential at $x = 0$ and $x = L$ (Barrier Length) can be expressed as

$$\frac{\partial n_p(x,y,t)}{\partial x} = 0, (p = e, i, n, \bar{\varepsilon} \ and \ V)$$

(2.6)

where e, i, n and $\bar{\varepsilon}$ illustrate the electrons, ions, neutrals (metastables and excimers) and electron mean energy. The Dirichlet boundary conditions are employed for the physical boundaries, i.e., AB and CD [14, 15] as displayed in figure 1. The flux of the charged particle species, electrons, electron energy density and neutrals at the solid dielectric boundaries are evaluated by using the modified boundary conditions for the atmospheric pressure discharges and can be written as

$$\Phi_p . \hat{n} = (2\beta - 1) \text{sgn}(q_p) \mu_p E_p^{eff} . \hat{n} n_p(x,y,t) + \frac{1}{2} v_{th,p} n_p(x,y,t)$$

$$\Phi_e . \hat{n} = -(2\beta - 1) \mu_e \vec{E_e} . \hat{n} n_e(x,y,t) + \frac{1}{2} v_{th,e} n_e(x,y,t) - \beta \sum_p \gamma_p \Phi_p . \hat{n}$$

$$\Phi_\varepsilon . \hat{n} = -(2\beta - 1) \frac{5}{3} \mu_e \vec{E} . \hat{n} n_\varepsilon(x,y,t) + \frac{2}{3} v_{th,e} n_\varepsilon(x,y,t)$$

$$\Phi_n . \hat{n} = \frac{1}{2} v_{th,n} n_n(x,y,t)$$

(2.7)

where $\hat{n}$ is the normal vector pointing towards the dielectric barriers; Here E_p^{eff} is the effective electric field for the particular ionic species and the $v_{th,p}$ is the thermal velocity of discharge species, defined as $v_{th,p} = \sqrt{\frac{8k_B T_p}{\pi m_p}}$, here k_B is the Boltzmann constant, T_p is the gas species temperature and m_p is the particle species mass. The $v_{th,p}$ exhibits the thermal velocity of discharge species of gas, which is assumed at room temperature (300 K). The integer β is set to one if the drift velocity is directed towards the dielectric barriers and to zero, otherwise

$$\beta = \begin{cases} 1 & \text{sgn}(q) \mu \vec{E} . \hat{n} > 0 \\ 0 & \text{sgn}(q) \mu \vec{E} . \hat{n} \leq 0 \end{cases}$$

(2.8)

where γ_p represents the secondary electron emission coefficient for the ionic species. The secondary electron emission coefficient for atomic and molecular helium ions is 0.1 in pure helium gas and 0.01 for all ionic species in He-N_2 gas. A sinusoidal oscillating voltage is applied on the large flat plate electrodes, thus imposing Dirichlet boundary conditions as

$$V = \begin{cases} V_0 \sin(2\pi f t) & \text{at driven electrode} \\ 0 & \text{at grounded electrode} \end{cases}$$

(2.9)

where V_0 is the amplitude of the applied voltage on the driven electrode, f is the driving frequency and t is the time elapsed during the discharge progress. The list of

the chemical reactions between the active discharge species are described in the tables 2.1 and 2.2 with their reaction rates and source references.

Table 2.1: List of chemical reactions with reaction rates in pure helium gas

No	Symbolic Form	Reaction Rate	Source
R_1	$He + e^- \rightarrow He^+ + 2e^-$	Boltzmann Solver (BOLSIG+)	[16]
R_2	$He + e^- \rightarrow He^* + e^-$	Boltzmann Solver (BOLSIG+)	[16]
R_3	$He^+ + 2He \rightarrow He_2^+ + He$	$1.5 \times 10^{-31} \ cm^6 \ s^{-1}$	[17]
R_4	$He^* + He^* \rightarrow He^+ + He + e^-$	$2.9 \times 10^{-9} \ cm^3 \ s^{-1}$	[19]
R_5	$He^* + He^* \rightarrow He_2^+ + e^-$	$2.0 \times 10^{-9} \ cm^3 \ s^{-1}$	[21]
R_6	$He^* + e^- \rightarrow He + e^-$	$2.9 \times 10^{-9} \ cm^3 \ s^{-1}$	[20]
R_7	$He^+ + e^- + e^- \rightarrow He + e^-$	$7.1 \times 10^{-20} \ cm^6 \ s^{-1}$	[18]
R_8	$He^+ + He + e^- \rightarrow He + He^*$	$1.0 \times 10^{-27} \ cm^6 \ s^{-1}$	[17]
R_9	$He_2^+ + e^- \rightarrow He^* + He$	$5.3 \times 10^{-7} \ T_e^{-0.5} \ cm^3 \ s^{-1}$	[20]
R_{10}	$He_2^+ + He + e^- \rightarrow 3He$	$2.0 \times 10^{-27} \ cm^6 \ s^{-1}$	[17]
R_{11}	$He^* + 2He \rightarrow He_2^* + He$	$1.3 \times 10^{-33} \ cm^6 \ s^{-1}$	[24]
R_{12}	$He_2^* + He_2^* \rightarrow He_2^+ + 2He + e^-$	$1.5 \times 10^{-9} \ cm^3 \ s^{-1}$	[17]
R_{13}	$He^* + He_2^* \rightarrow He^+ + 2He + e^-$	$2.5 \times 10^{-9} \ cm^3 \ s^{-1}$	[17]
R_{14}	$He^* + He_2^* \rightarrow He_2^+ + He + e^-$	$2.5 \times 10^{-9} \ cm^3 \ s^{-1}$	[17]

As the molecular nitrogen impurities are introduced in pure helium gas, then the helium gas atoms and excited particles interact with the nitrogen molecules and the major chemical reaction scheme for the construction and destruction of discharge species is represented in the following table as

Table 2.2: List of chemical reactions with reaction rates in He-N$_2$ gas

No	Symbolic Form	Reaction Rate	Source
R_1	$N_2 + e^- \rightarrow N_2^+ + 2e^-$	$4.5 \times 10^{-7} \ T_e^{-0.3} \ e^{-1.85 \times 10^5 / T_e} \ cm^3 \ s^{-1}$	[22]
R_2	$N_2^+ + e^- + e^- \rightarrow N_2 + e^-$	$5.6 \times 10^{-27} \ T_e^{-0.8} \ cm^6 \ s^{-1}$	[22]
R_3	$N_2^+ + e^- \rightarrow N + N$	$2.0 \times 10^{-7} \ cm^3 \ s^{-1}$	[21]
R_4	$He^* + N_2 \rightarrow He + N_2^+ + e^-$	$5.0 \times 10^{-11} \ cm^3 \ s^{-1}$	[11]
R_5	$He^* + N_2 + He \rightarrow He + N_2^+ + e^-$	$3.3 \times 10^{-30} \ cm^6 \ s^{-1}$	[21]
R_6	$He_2^+ + N_2 \rightarrow 2He + N_2^+$	$1.1 \times 10^{-9} \ cm^3 \ s^{-1}$	[21]
R_7	$He_2^+ + N_2 + He \rightarrow 3He + N_2^+$	$1.3 \times 10^{-29} \ cm^6 \ s^{-1}$	[21]
R_8	$He_2^* + N_2 \rightarrow 2He + N_2^+ + e^-$	$3.0 \times 10^{-11} \ cm^3 \ s^{-1}$	[11]

Some reactions in these tables are a function of the electron temperature T_e, as displayed in tables 2.1 and 2.2. The electron temperature T_e is calculated from the solution of the electron energy density equation considering all the elastic, inelastic energy losses due to the electron impact reactions and joule heating. So, the rate coefficients and transport coefficients of electron impact reactions are dependent on the electron mean energy and modified after every time step (Δt). The electron mobility and the reaction rate coefficients of excitation and ionization are evaluated with the freeware Boltzmann solver BOLSIG+ [16]. The local field approximation is

employed for the ionic species in which the transport and rate coefficients are regarded as a function of electric field. The reduced diffusion coefficients and mobility of ionic species, i.e., He^+, He_2^+ and N_2^+ in pure helium and He-N_2 gases are calculated from the data available in [23]. The diffusion coefficients of the neutral species (metastables and excimers), D_{He^*} =4.116 cm^2 s^{-1}, $D_{He_2^*}$ =2.029 cm^2 s^{-1} [22], are used in the present numerical study. Charges are accumulated on the surface of momentary dielectric barriers in different phases during the atmospheric pressure discharge operation, so the surface charge density σ is taken into account for the upper (U) and lower (L) dielectric barriers by using Gauss's law [24], which can be evaluated by the equation:

$$\sigma(x, y_{U,L}, z, t) = \mp \varepsilon_0 \frac{\partial V(x, y_{U,L}^{\pm}, t)}{\partial y} \pm \varepsilon_0 \varepsilon_r \frac{\partial V(x, y_{U,L}^{\mp}, t)}{\partial y}$$

(2.10)

where V is the imposed electric potential. The Scharfetter-Gummel exponential scheme [25] is employed for the discretization of transport terms in the continuity equations of discharge species and electron energy density.

3. Results and discussion

In atmospheric pressure discharge, the occurrence of sharp increase in current takes place at the event breakdown, which is an essential feature of self-sustaining dielectric barrier discharges in the alternate cycles of an oscillating sinusoidal source. The number of oscillating cycles for the achievement of stationary-state of discharge plasma depends on the initial distribution of discharge species. In present two-dimensional fluid model, the complete breakdown for the formation of homogeneous glow and filamentary discharge is dependent on the initial density of quasi-neutral plasma at constant atmospheric pressure. If the initial density of discharge plasma is quite small for fluid model simulations, the time for accomplishment of steady-state breakdown is longer and vice versa. The different case studies in this paper consider a quasi-neutral plasma with an initial density of electrons and ions ~ 10^8 cm^{-3}.

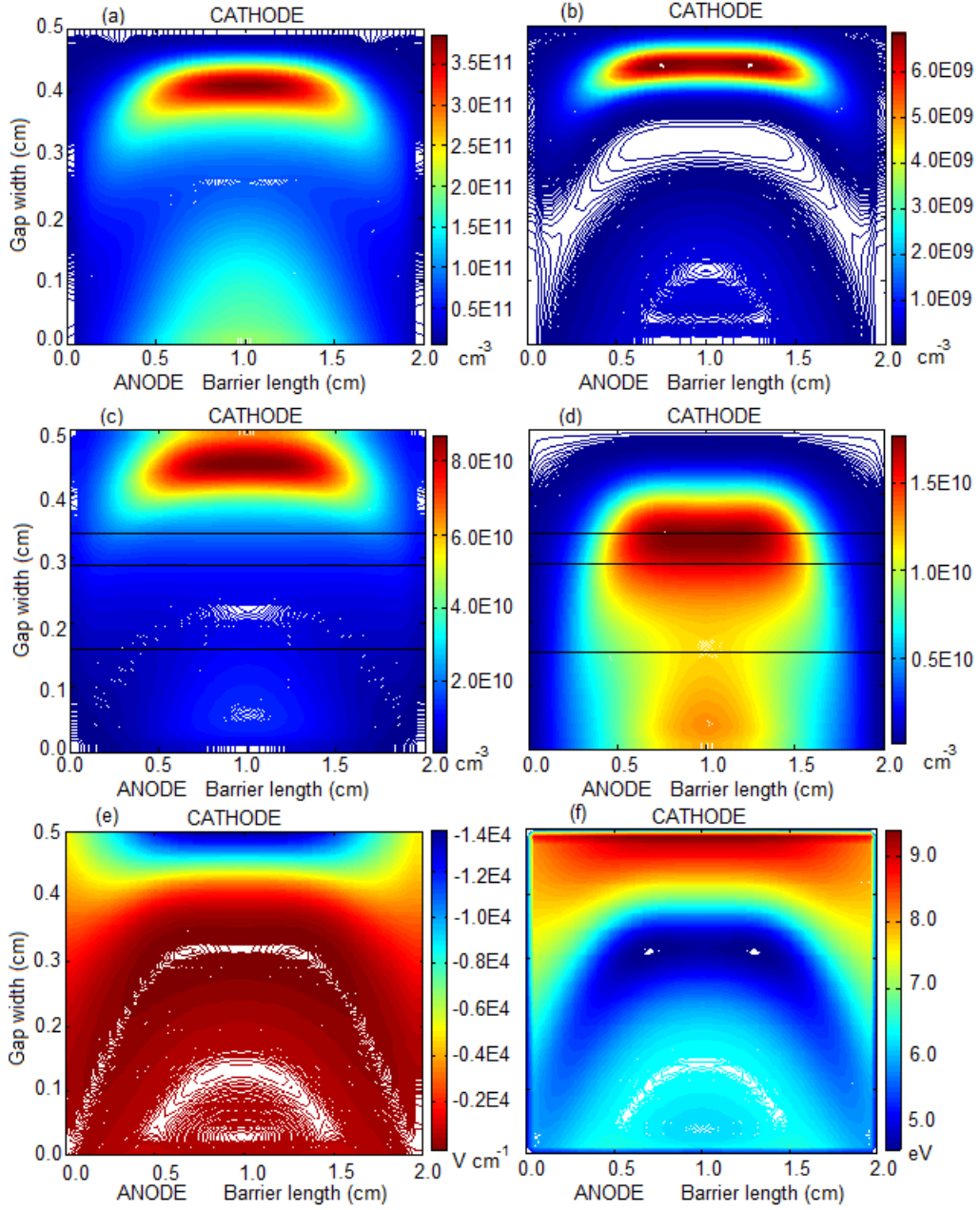### 3.1. Spatial profiles of discharge parameters in pure helium gas

FIG. 2. Spatial distributions of He*, He$^+$, He$_2^+$, electrons, axial electric field (E$_y$) and electron mean energy for f = 20 kHz, ε_r = 7.5, γ_p = 0.1 and V_{appl} = 2.1 kV in pure helium gas.

At atmospheric pressure, any gas contains thousands of positive and negative charge particles per cm^{-3}, for example, due to radiation in the atmosphere. These charged particles act as seed in the parallel plate dielectric barrier discharge (DBD) reactor and produce further ionization after the application of external imposed sinusoidal potential. When these seed electrons pass through the gas, they collide with the gas atoms and molecules, and reactions occur, such as excitation, ionization and other consequential chemical reactions. The sudden progressive chemical change in these activities is emanated in the reactor gap, when the external imposed potential is greater than the breakdown potential of helium gas in the presence of dielectric barriers with a specific permittivity. In pure helium gas, the excitation rate of metastables is quite large and they are quickly transformed into atomic and molecular ionic species through various stepwise ionization channels after the breakdown of

helium gas. The discharge current rapidly reaches its maximum value after breakdown and the typical spatial distributions of discharge parameters are shown in figure 2 during evolution of uniform glow discharge plasma. The twin-peak distribution of metastables is in contrast to other discharge species as displayed in figure 2 (a). One peak occurs due to the direct excitation near the cathodic barrier with density magnitude $\sim 3.0 \times 10^{11}$ cm^{-3} and other is a residual from the previous discharge pulse with density magnitude $\sim 1.5 \times 10^{11}$ cm^{-3}. Direct ionization produces atomic helium ions, which are rapidly converted into molecular helium ions using the main channel of three body reaction, i.e., R$_3$ of table 2.1. Thus, the density of atomic helium ions is smaller than the molecular helium ions as displayed in figure 2 (b, c).

In helium gas, the length of glow discharge plasma comprises of four distinct regions, such as cathode fall layer (CFL), negative glow (NG), Faraday's dark space (FDS) and positive column (PC), which are evident from the spatial distributions of electrons, molecular helium ions and axial electric field in figure 2 (c, d, e) and this has been discussed as a benchmark criterion for the identification of uniform glow discharge plasma in literature [8 - 11]. In CFL, the greatest density of helium ionic species and strength of axial electric field are evolved and become significantly small away from the cathode as shown in figure 2. The axial electric field has a sharp distorted profile in the CFL with a magnitude of -1.4×10^4 V cm^{-1}, which minimizes in the NG region, and again increases its strength in PC. The spatial structure of axial electric field in figure 2 (e) for the glow discharge plasma is perfectly consistent with the theoretical description available in the literature [10, 29]. Newly formed electrons are accelerated in the cathode fall to high energies due to the existence of higher electric field and amplify chemical interactions at the edge of CFL, which act as a strong source of ionization. The gain of electron mean energy is higher than the losses in CFL and these losses become considerably more in the negative glow region. This can be justified from the spatial distribution of electron mean energy in these regions, which exhibits that the it is varied from 9.0 to 3.0 eV as shown in figure 2 (f). After this strong decline in the distribution of electron mean energy, the electrons again start gaining energy in the positive column. The electron density becomes negligibly small on the surface of cathodic barrier and starts rising from the middle of CFL. The electron flux is greatly enhanced at the end of cathode fall layer and ultimately, the electrons acquire a density peak of $\sim 1.5 \times 10^{10}$ cm^{-3} in the negative glow region. The evolution of FDS shows that the density of molecular helium ions is greater than electrons and the smallest values of charged particles and axial electric field are obtained in this particular region. The fourth region, usually called as the positive column, contains a small percentage of energetic electrons, which are responsible to produce the excitation and ionization. The ionic species are repelled from the anode and the electrons attract towards the anode in the positive column, which eventually forms a quasi-neutral and weak plasma in this region because of smaller electron energy. So, the pre-ionization level is achieved in PC before the next breakdown pulse from the production sources of electrons. A qualitative interpretation of light emission pattern can be described from the mentioned four distinct regions of glow discharge plasma in pure helium gas.

4. Behaviour of uniform discharge plasma in He-N$_2$ gas

Generally, the presence of impurities cannot be ignored at atmospheric pressure. The present numerical simulation modelling study deals with the variable quantities of N$_2$ impurities, such as 20 and 50 ppm N$_2$ in pure helium gas, which are able to form

uniform and filamentary discharge plasmas under different operating conditions. The N_2 impurity molecules can vigorously react with helium metastables to produce ionization by the Penning process, which enhances the quenching of metastables. The threshold potential for the formation of uniform glow discharge plasma in He-N_2 gas is consequently reduced by few hundreds of volts (0.65 kV) from the preceding section of pure helium gas. If the magnitude of applied voltage is further reduced from this limit, the breakdown will be significantly weak and the Townsend discharge mode (lower ionization mode or dark discharge) occurs. The magnitude of applied voltage must exceed the breakdown voltage of gas for the successful development of electron avalanche in the reactor gap, which is essential for the evolution of atmospheric pressure glow discharge. The breakdown voltage depends on the gas mixture, relative permittivity and width of dielectric barrier, discharge gap width and pressure [1]. The difference ($\Delta V = V_{appl} - V_{breakdown}$) between the applied and breakdown voltage is termed as overvoltage. If the magnitude of the overvoltage is increased from 15 to 20 % of threshold breakdown voltage, a filamentary discharge mode prominently appears. In this study, we first describe the spatial evolution of uniform glow discharge plasma in He-N_2 gas in which nitrogen impurities act as a catalyst for reducing the breakdown voltage of gas than the pure helium gas. The increment in the magnitude of external applied voltage is varied in different cases to differentiate the prominent role of overvoltage, which is the main factor influencing the formation of a non-equilibrium uniform glow or filamentary discharge plasma. We consider a range of conditions, and the influence of these conditions is examined during the evolution of filamentary discharge plasma in the breakdown and decay phases of a half cycle. The filamentary discharge plasma appears in the form of thick and thin conducting channels, depending on the source driving frequency, and the single homogeneous conduction channel emerges in case of uniform glow discharge plasma between the dielectric barriers.

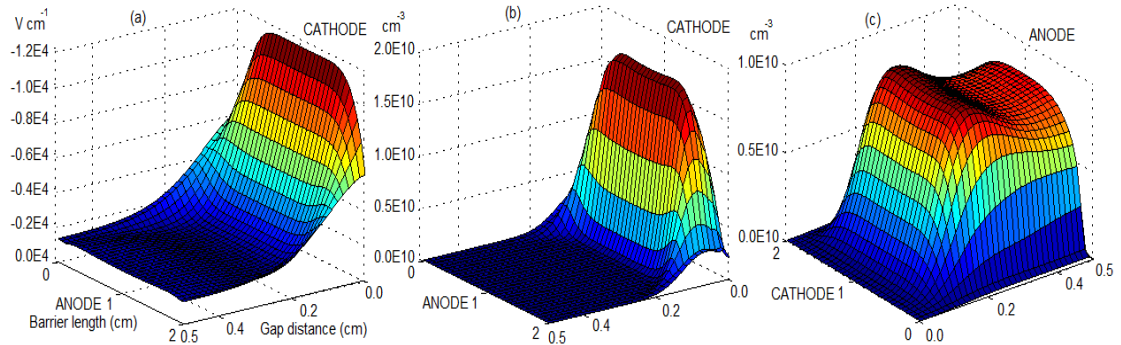## 4.1. Spatial profiles of uniform glow discharge

FIG. 3. Spatial structures of axial electric field, He$_2^+$ ions and electrons density for $f = 20$ kHz and $V_{appl} = 1.45$ kV with 50 ppm N_2 impurities.

Here, we identify the optimal value of overvoltage for the formation of homogeneous uniform glow discharge plasma. If the magnitude of the applied potential is somewhat smaller than breakdown threshold under similar operating conditions, the probable mode of discharge plasma will be Townsend or weak discharge rather than glow discharge plasma. The most important phase of a discharge current pulse is breakdown, in which the Townsend ionization mechanism is dominant, and the outcome is a diffuse electronic avalanche with the current growing rapidly in the uniform glow discharge phase. The internal structure of discharge plasma is illustrated by the spatial distributions of axial electric field, molecular helium ions and electron

densities at the maximum discharge current density, shown in figure 4. The cathode fall region is observed with a strong distortion in the electric field and molecular helium ionic density along with negligible density of electrons as shown in figure 3 (a, b, c). The positive column is essential to distinguish the uniform character of the discharge plasma, because it traps sufficient number of electrons and ions for the next discharge current pulse. The uniform structure of the electron density in the positive column shows that the Townsend ionization is responsible for the diffuse glow discharge, rather than the streamer breakdown mechanism, in which constricted channels of conduction of charge carriers develop in the breakdown phase. The streamer breakdown is ignited when the overvoltage increases from the above mentioned percentage of breakdown voltage. The next section provides the consequences of higher magnitudes of overvoltage in the Penning mixture of He-N_2 gas.
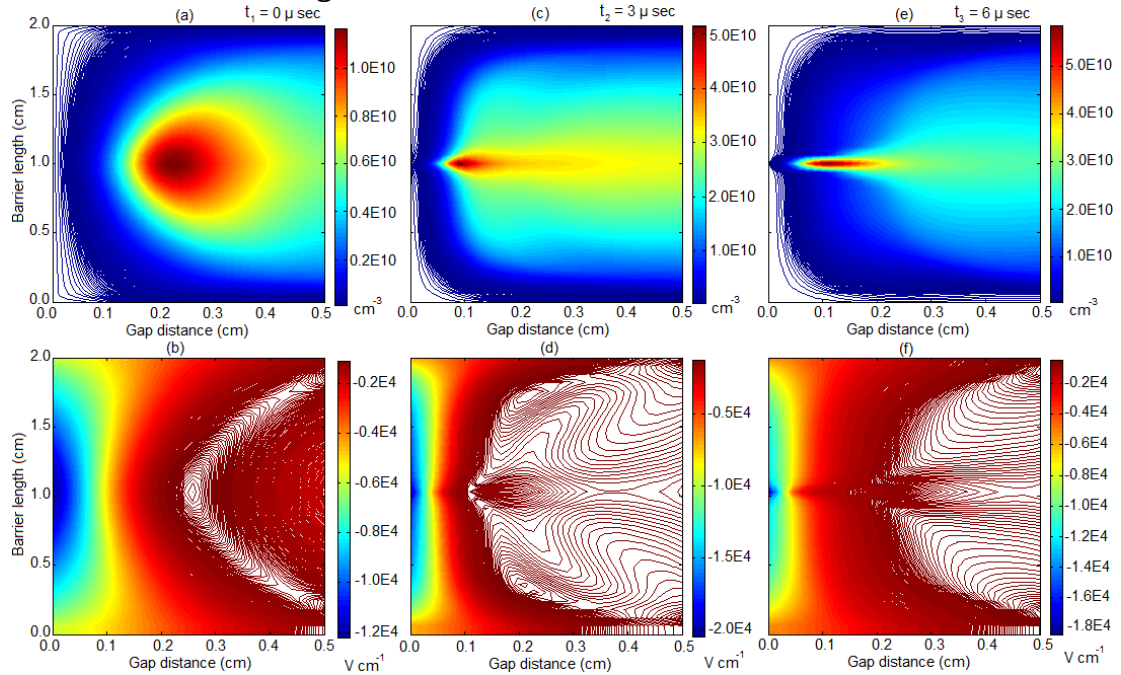
4.2. Effect of overvoltage in APD[3]

FIG. 4. Spatio-temporal evolution of electrons density and axial electric field for f = 20 kHz, ε_r = 9.0, RC = 5.0×10^{-6} cm^3 s^{-1}, γ_p = 0.01 and V_{appl} = 1.6 kV with 50 ppm N_2 impurities.

In order to compare the effect of overvoltage, the amplitude of external imposed voltage is raised by 0.15 kV from the earlier discharge plasma case in He-N_2 gas and results in the creation of constricted filamentary discharge. The development of space charge from the electronic avalanche is essential to the birth of streamers. In the breakdown phase, the electrons are emitted from the cathode and migrate rapidly towards the anode barrier, while the ions form a positive space charge towards the cathode. This establishes an electric field in this region, which increases towards the cathode barrier. The streamer originates in a short time with a rapid transport of space charge towards the cathodic barrier. Streamer formation occurs at some distance from the anode, depending on the operating parameters, and immediately extends towards the cathode barrier. Streamer breakdown appears as the dominant mechanism due to the effect of higher magnitude of overvoltage, which forms a filamentary glow

---

[3]   APD: Atmospheric pressure discharge

discharge plasma with a distorted axial electric field and a thin cathode fall layer in the presence of positive column. To visualize the evolution of the filamentary structures, we consider the electron density and electric field at three specific time instants (t_1, t_2 and t_3). The cathodic and anodic dielectric barriers are not shown in the spatial profiles, and their polarities of course vary with the external applied potential. Experimental studies [13, 26] show that the avalanche breakdown initiates at the position of the cathode fall layer from the preceding discharge, and in the center of the reactor gap. Since the gas breakdown activity begins at time $t_1 = 0$ μs in the middle of gap, an avalanche is formed by the dynamic response of electrons along with growing electric field. The figure 4 (a, b) corresponds to the instant of breakdown initiation with a maximum electron density of ~ 1.0×10^{10} cm^{-3} and axial electric field E_y = -1.2×10^4 V cm^{-1} at t_1. The immediate spatial expansion of electron avalanche is produced by the drift of accelerated electrons and ions, and the streamer breakdown phase is fully developed with the production of charge carriers from multiple channels. The dielectric barriers are employed to accumulate the surface charge with the conduction of charge carriers, which becomes less due to the collection of ions only at the cathode barrier. This causes a flow of electrical current in the gas and immediately, it acquires a peak value at $t_2 = 3$ μs. From $t_1 \rightarrow t_2$, another opposing potential is developed in DBD by the accumulation of surface charge, which opposes the external imposed potential and controls the flow of current. This property of dielectric barriers prevents the creation of arcs. At t_2, the distorted distribution of axial electric field in CFL is observed with a greatest value E_y = -2.0×10^4 V cm^{-1} in the constricted region, where the density of electrons is still increasing, as shown in figure 4 (c, d). The space charge is formed by the spread and contraction of charge carriers in the particular region and it is negative at the tip of streamer due to higher mobility of electrons. This develops a non-uniform electric field in the mentioned region and becomes very small at the anode barrier. The peak of electron density is obtained at the head of a filament in the negative glow region and immediately falls to very small values in its proximity except in the axial direction, indicating the effect of larger drift flux than diffusion flux. In the preceding section 4.1, the uniform structure of APD is persists at the maximum current density, but the constricted filamentary distribution of discharge plasma appears only in the present case, which illustrates the influence of magnitude of overvoltage in the formation of filamentary glow discharge plasma. Thus the streamer breakdown is considered as the cause for the establishment of single filament at 20 kHz. The compressed layer of ionic species is responsible for the secondary emission of electrons from the cathode barrier and these electrons are accelerated by the non-uniform electric field in cathode fall. In the afterglow phase of the current pulse at $t_3 = 6$ μs, electron production is extinguished and the density reaches its peak value ~ 6.0×10^{10} cm^{-3} but the axial electric field start decreasing after t_2 in contrast to electron density and its axial strength falls to -1.8×10^4 V cm^{-1} as exhibited in figure 4 (e, f). In a normal uniform glow discharge, the electron density is continuously increased until it reaches a maximum at the location of next cathode fall layer. This does not happen in the present case because of impact of higher recombination coefficient of nitrogen impurity ions, which inhibits the rise in the electron density after t_3 and reduces its value in the pre-ionization phase of next discharge current pulse. So the next discharge current pulse will definitely be in the filamentary form. The rise in electron density at t_2 is five time higher than t_1 but the increment of electron density becomes significantly slow in the afterglow phase at t_3. Although, the magnitude of axial electric field is approximately double from t_1 to t_2, and the rate of fall in magnitude is substantially small in the afterglow phase at t_3. The

evolvement of uniform and filamentary structures in sections 4.1 and 4.2 exhibit that they are formed due to the influence of distinct magnitudes of overvoltage. It is important to note that the values of time instants (t_1, t_2, ..) are different in different sections of this paper.

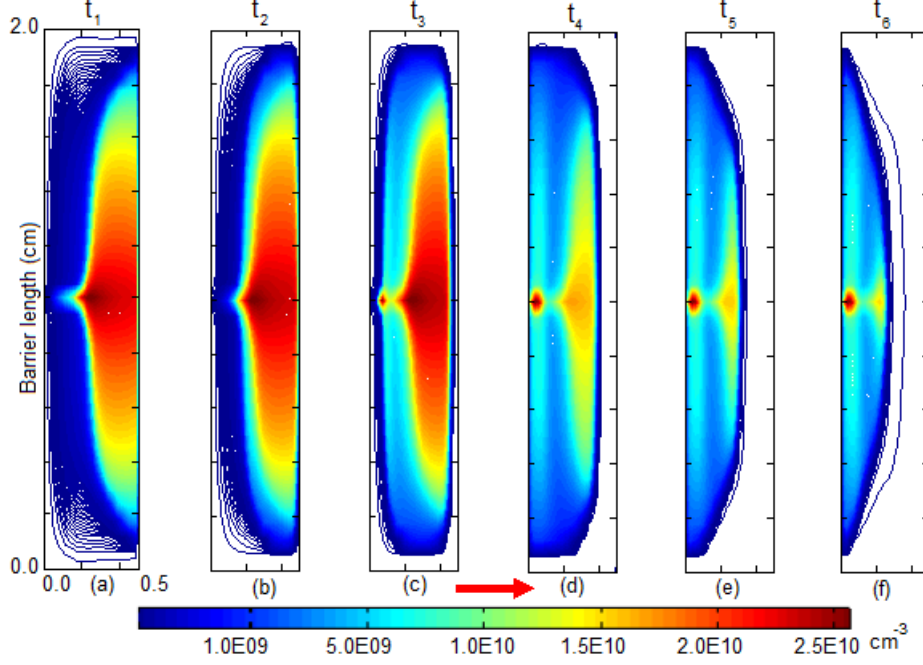## 4.3. Influence of higher recombination coefficient of N_2^+ ions

FIG. 5. Spatio-temporal evolution of electrons density in the afterglow phase for f = 20 kHz, ε_r = 9.0, RC = 5.0×10^{-6} cm^3 s^{-1} and V_{appl} = 1.6 kV with 50 ppm N_2 impurities.

In the previous section, we discussed the influence of overvoltage on discharge uniformity. A second important parameters is the rate of recombination with molecular nitrogen ions, which is important in the afterglow. Ionization processes, such as direct and Penning ionization are dominant in the breakdown phase, which forms a glow or filamentary discharge plasma but the recombination of N_2^+ ions plays an key role in the decay phase of discharge current pulse, rather than the destruction rates of helium ionic species (He^+ and He_2^+). A uniform glow discharge will occur if a sufficient amount of electron density exists before the next discharge current pulse. If the recombination coefficient of molecular nitrogen impurity ions is increased to 5.0×10^{-6} cm^3 s^{-1} from the literature value 2.0×10^{-7} cm^3 s^{-1}, the destruction of electrons becomes greater in the decay phase and the next discharge pulse will be in the filamentary form. This can be observed by the spatial distributions of electron density before and after the polarity reversal of the conduction discharge current density in the decay phase. Three instances of spatial distributions of electron density are considered before and three after polarity reversal of conduction discharge current pulse with an equal increment in the time interval of ~ 1.25 μs between any two adjacent events from t_1 to t_6 as shown in figure 5. In decay phase, the electrons are destroyed by the effect of higher dissociative recombination coefficient than the normal uniform discharge plasma and its density value reduces to ~ 1.0×10^{10} cm^{-3} at t_3 as shown in figure 5 (a, b, c). Since the maximum surface charge density is accumulated on the cathodic barrier before the polarity reversal of external applied potential and it enhances the creation of filamentary distribution of electrons in the decay phase at t_3. After the polarity reversal of discharge current pulse at t_4, the

distribution of electrons density is further divided into two layers, which exhibit the strong and weak filaments on both sides due to the existence of variable localized density gradients as illustrated in figure 5 (d, e). This immediate movement of electrons develops a small current after polarity reversal of external applied potential and is often termed as residual current. It is evident from the spatial distributions of electrons density that the filamentary layers are trying to merge and the electrons squeeze in the smaller portion between dielectric barriers as exhibited in figure 5 (f). In normal uniform glow discharge, the density of electrons is not reduced to such a limit where such filamentation could form before and after polarity reversal of external applied potential. The source of filamentation is considered as Townsend ionization mechanism because of presence of small electric field, which is very high and distorted in the breakdown phase of filamentary glow discharge plasma. Therefore, the significance of higher recombination coefficient is in the pre-breakdown phase of filamentary discharge plasma. The number of filaments increases at smaller frequencies (< 20 kHz). This observation is consistent with previous simulation results in [13]. This shows the consistency of numerical simulation results and illustrates the origin of filamentation in the dielectric barrier discharges at atmospheric pressure.

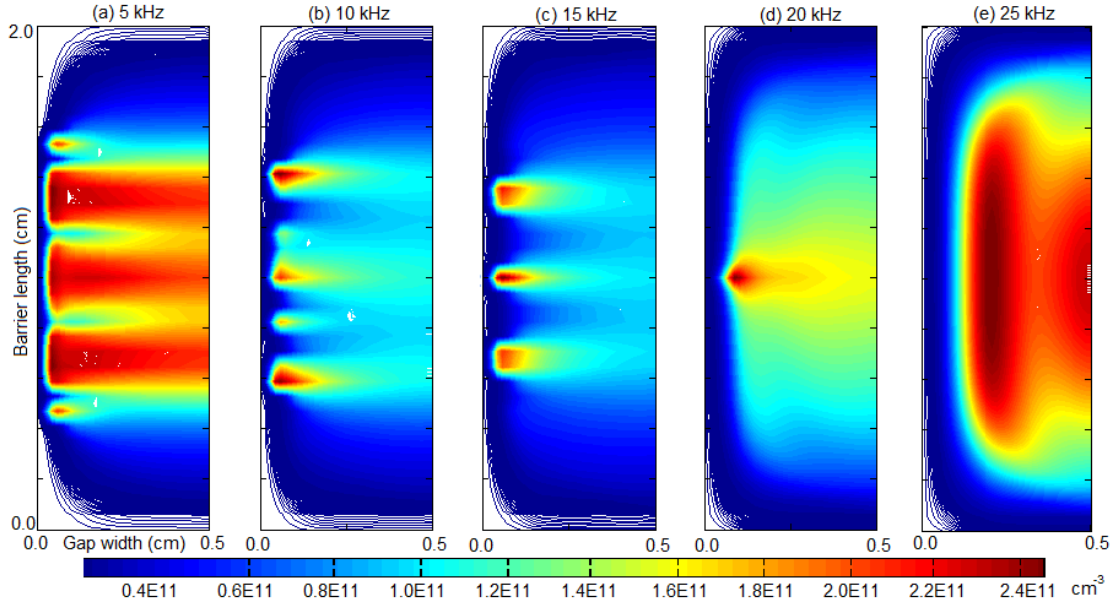## 4.4. Effect of driving frequency in Filamentary APD

FIG. 6. Effect of driving frequency for the distributions of electrons density at $f = 5 - 25$ kHz, $\varepsilon_r = 9.0$, RC = 5.0×10^{-6} cm^3 s^{-1} and $V_{appl} = 1.6$ kV with 50 ppm N$_2$ impurities.

It is important to investigate the effect of source driving frequency in the development of filamentary and uniform discharge plasma. Massines, et al. [9] showed that the behaviour of atmospheric pressure discharge is entirely different at lower frequencies (≤ 5 kHz) than higher frequencies: It is difficult to observe the stationary pattern in the mentioned lower frequency regime. With the use of self-consistent two-dimensional fluid model, a very strong asymmetric breakdown occurs in the lower frequency regime (< 7 kHz) due to longer time period of an oscillating cycle, which is confirmed with the spatial filamentary distribution of electron density at 5 kHz during the evolution of current density peak. At 5 kHz, the thin filaments are fused together in the bulk and emerge in the form of thick filaments than the surrounding filaments

as shown in figure 6 (a). These filaments are considered as the conducting channels in the filamentary glow discharge plasma. At 10 kHz, the radial and axial growth of filaments are minified in the breakdown phase, which outcome in the form of compressed filaments as shown in figure 6 (b). The comparison of filamentary distributions of electron density exhibits that the shift in frequency from 5 to 10 kHz amplifies the filamentation in the discharge plasma. The location of filaments remains the same in every cycle, which provides the consistent feature of emergence of non-uniform structure in the DBDs. Subsequently, the filaments are coalesced together at 15 kHz and this occurs due to the reduction in time period of driving frequency. The coalescence of filaments becomes further strengthen and the outcome is resulted into isolated single filament in the breakdown phase at 20 kHz under the similar operating conditions. The filamentary discharge plasma is completely extinguished at 25 kHz, which illustrates the transformation from filamentary to glow discharge plasma and which provides the evidence of the coalescence of filaments with the effect source driving frequency in the breakdown phase. It has been described that some form of compelling potential is always present between any pair of adjacent filaments. To determine such kind of potential between any pair of adjacent filaments, the potential is evaluated by using Coulomb's repulsive and Lorentz attractive forces, which shows that the former repulsive force is exceedingly greater than the Lorentz attractive force. This feature of filamentary dielectric barrier discharges is consistent and followed by the previous modelling results as discussed in [27, 28]. The intensity of gas breakdown is analyzed by the comparison of electron density from 5 to 25 kHz, which reduces from $\sim 2.5 \times 10^{11}$ to 2.0×10^{10} cm^{-3} as shown in figure 6. This shows that the filamentary mode of discharge plasma is transformed into uniform mode by the shift of frequency from 5 to 25 kHz. So, the evolution of uniform glow discharge plasma is more probable at higher frequencies as compared to small frequencies in the presence of Penning impurities. As the excimers play an important role in He-N$_2$ discharge plasma due to the Penning ionization process, so they are considered in the following simulation results with a quenching frequency of 1.0×10^6 sec^{-1}.

5. Behaviour of uniform atmospheric pressure discharge plasma
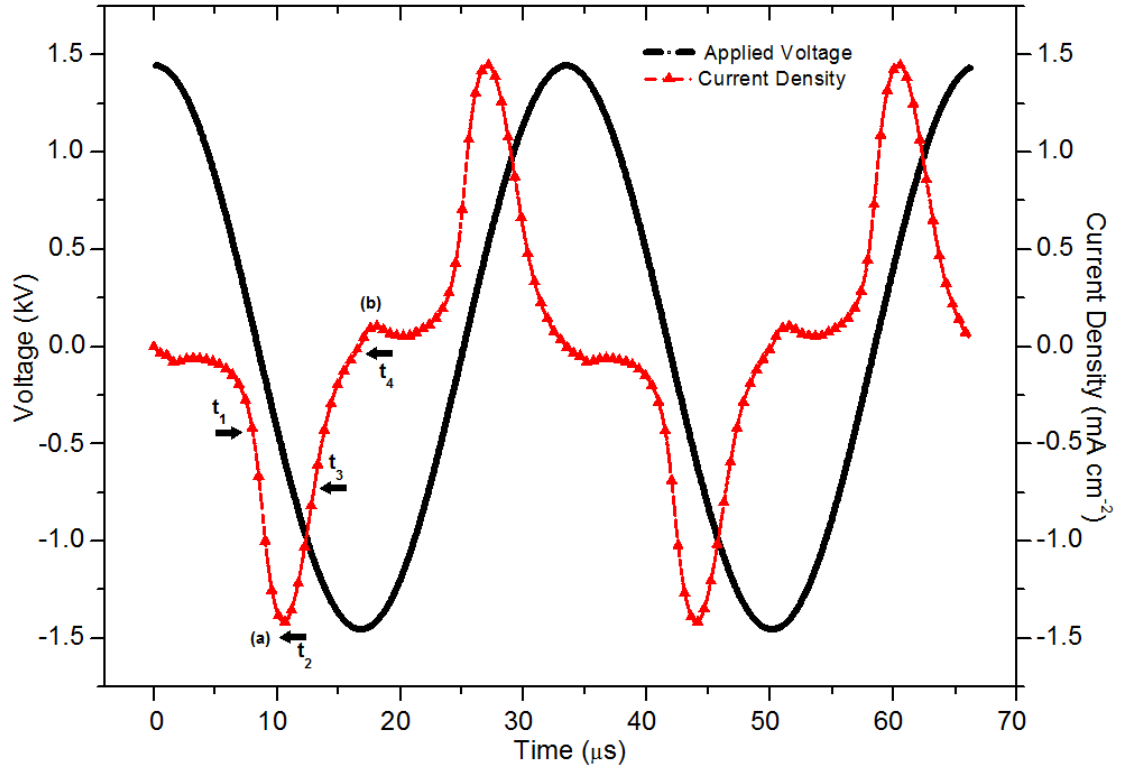
5.1. Electrical characteristics of APD

FIG. 7. V-I characteristics for the periodic stationary-state of APGD[4] for f = 30 kHz, ε_r = 7.5, γ_p = 0.01 and V_{appl} = 1.45 kV with 20 ppm N_2 impurities.

π

As the previous discussion provides the comparative analysis of spatial properties of non-thermal homogeneous uniform and filamentary discharge plasma at distinct frequencies. In order to investigate the temporal behavior, the analysis of electrical characteristics is shown with the voltage-current parameters for two consecutive cycles. The periodic stationary pattern in figure 7 shows that the higher (a) and lower (b) current density peaks are evolved per half cycle and the remaining discharge properties recur in consecutive cycles. The absorption of energy from the mean electric field is important for the accelerated charge carriers in the breakdown pulse, which results in ionization of neutral particles and ultimately, release of this energy in the afterglow phase. The state of homogeneous uniform glow discharge plasma is occurs at the peak of large current density and a very short time requires for the achievement of this phase than other phases as shown in figure 7. The trapped electrons in the positive column enhances a weak disturbance during the polarity reversal of external applied potential, which occurs in the form of small current peak (b), and termed as residual current. The residual current is immediately amplified at higher driving frequencies as compared to the lower frequencies in APDs due to strong trapping of stream of electrons.

5.2. Evolution of electrons density in uniform APD

In case of uniform glow DBDs, an in-depth understanding of discharge current pulse is developed by examining the spatio-temporal distributions of electron and surface charge densities at specific time instants (t_1, t_2, t_3 and t_4), which provide a physical description of homogeneous uniform glow discharge plasma in different phases of a discharge current pulse. These simulation characteristics are precisely described with the help of two-dimensional fluid model in helium gas with 20 ppm N_2 impurities.
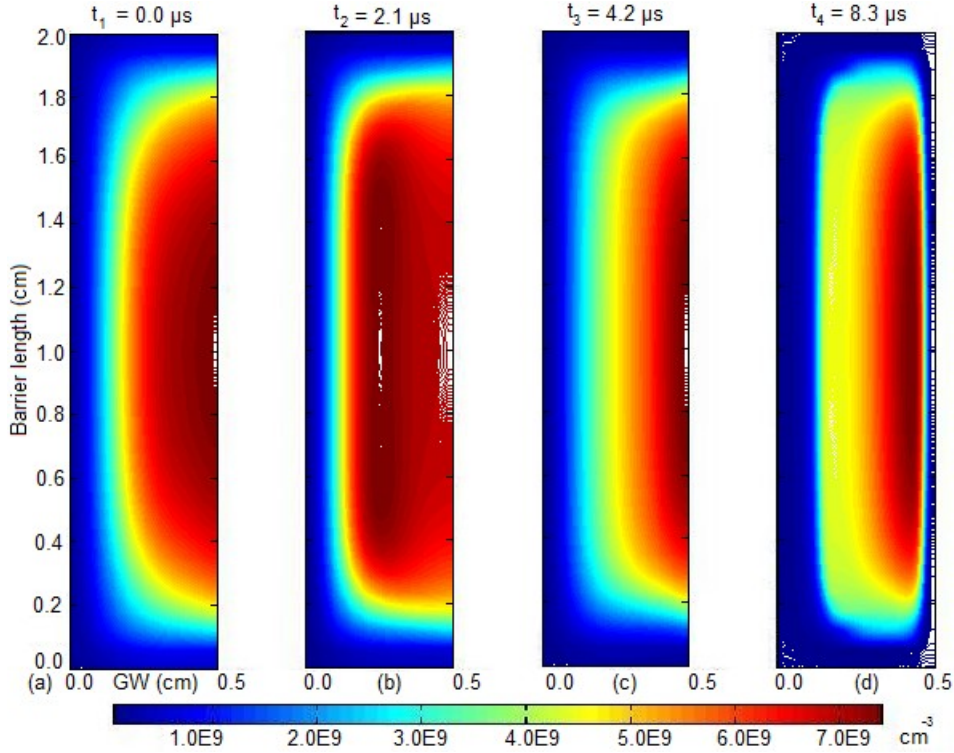
---

[4]   APGD: Atmospheric pressure glow discharge

FIG. 8. Spatio-temporal profiles of electron density for f = 30 kHz, ε_r = 7.5, γ_p = 0.01, Barrier width = 0.1 cm and V_{appl} = 1.45 kV with 20 ppm N_2 impurities.

The quantitative analysis of electrons is performed from the electrical profile of negative discharge current pulse as shown in figure 8. Figure 8 (a) represents the earlier instant before initiation of breakdown at t_1 = 0 with its numerical value ~ 3.0×10^9 cm^{-3}, while electrons are concentrated between the center of reactor gap and the anode barrier. This demonstrates that the electron avalanche starts from the middle of gap after the breakdown of gas and spreads rapidly in the radial and axial directions during the advancement from time instant ($t_1 \rightarrow t_2$). Secondary electrons are emitted from the cathodic barrier by the bombardment of ionic species in breakdown phase, which furthers the creation of intense ionization in the cathode fall. The peak of electron density develops in the negative glow region. This phase corresponds to the Townsend breakdown mechanism because of the high electric field and emergence of uniform distribution of electrons throughout the reactor gap as shown in figure 8 (b). The peak of conduction discharge current density is reached, when the electron density acquires its temporary peak in the negative glow region along with other three distinct regions. In the decay phase of the discharge current pulse from t_2 to t_3, the cathode fall collapses and mean electric field declines. The rate of production of electrons consequently falls in the decay phase of discharge current pulse but the overall density of electrons increases continuously at t_3. The electron energy losses, such as elastic and inelastic losses and joule heating effect, are considered as dominant in the afterglow phase, while they are not exactly balanced by the production processes but act to reduce the productive yield of electrons to some extent. Finally, the electron density approaches to its maximum value ~ 7.0×10^9 cm^{-3} at t_4 = 8.3 μs at the position of forthcoming cathode fall layer for the next breakdown pulse as prominently shown in figure 8 (d). The immediate ($t_1 \rightarrow t_2$) and steady ($t_2 \rightarrow t_4$) advancement of electron density in the discharge current pulse is an essential feature of homogeneous uniform glow discharge plasma at atmospheric pressure,

indicating that the violation of this constraint outcomes in the form of some other form of discharge plasma because a substantial quantity of electrons in the pre-breakdown phase plays an important for the development of uniform glow discharge plasma. The electrical and spatio-temporal profiles of electrons are enclosed in the figures 7 and 8, which enhance an understanding of fundamental characteristics of dielectric barrier discharges.
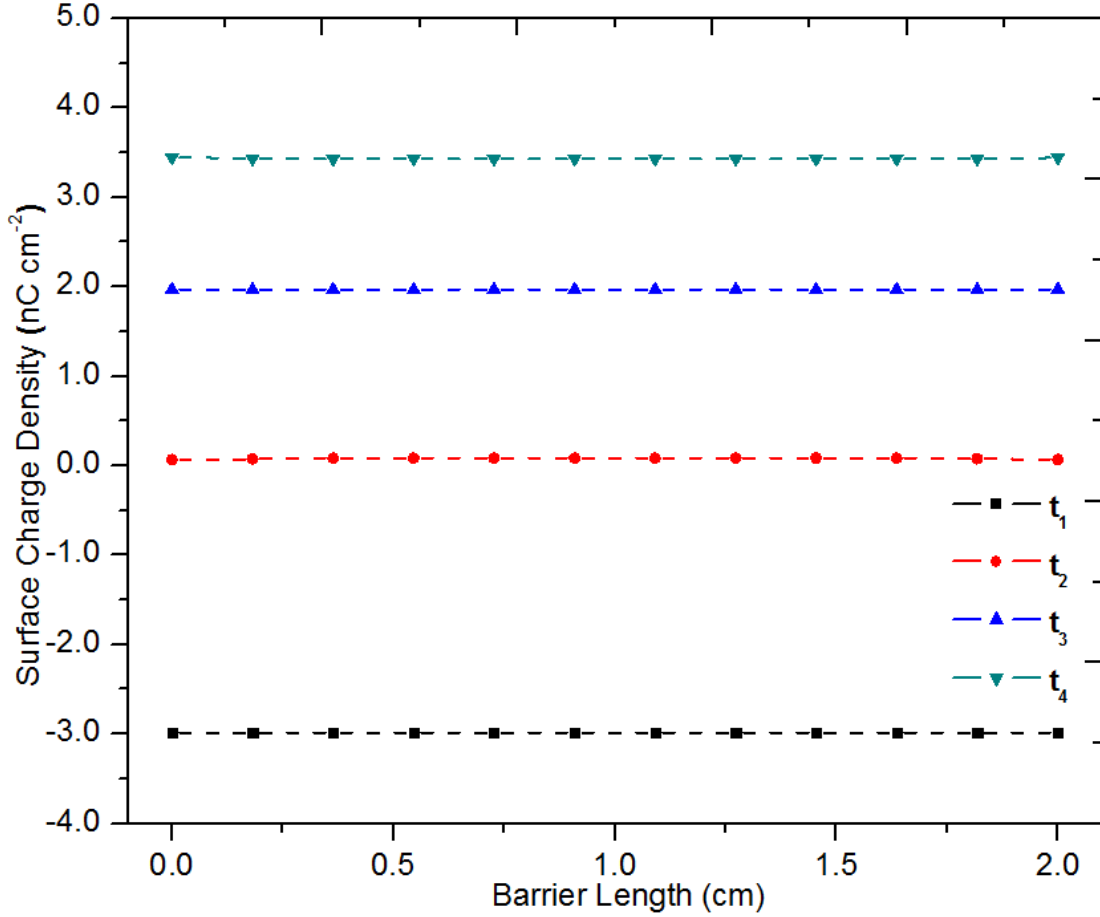
5.3. Spatio-temporal evolution of surface charge density

FIG. 9. Spatio-temporal evolution of surface charge density for f = 30 kHz, ε_r = 7.5, γ_p = 0.01, Barrier width = 0.1 cm and V_{appl} = 1.45 kV with 20 ppm N_2 impurities.

The attachment of dielectric barriers with the flat electrodes is crucial for the formation of uniform and regularly patterned atmospheric pressure discharges, whereas the characteristics of barrier material are described by the evolution of surface charge on dielectric barriers. The surface charge density is calculated by using Gauss's law, which mainly depends on the relative permittivity and width of the dielectric barrier along with an external imposed potential, and described in Eq. (2.10) in section 2. The behaviour of surface charge density is dynamically altered on the cathodic and anodic dielectric barriers during the oscillating discharge current pulse at previously mentioned time instants (t_1, t_2, t_3 and t_4). Figure 9 exhibits the distribution of surface charge density on the powered cathodic dielectric barrier at four distinct time instants. The deposition of surface charge establishes a memory effect that is an essential characteristic feature of dielectric barrier discharges, while the electrons and ions trapped in the PC play an important role to determine the memory effect in case

of dielectric barrier discharges [30]. Earlier the initiation of breakdown at $t_1 = 0$ μs, the dielectric barrier is negatively charged due to the memory effect of the precedent breakdown pulse. After breakdown, the accumulation of positive charge on the surface of cathodic dielectric barrier is developed by the ejection of electrons through multiple channels, such as external imposed potential and secondary emission of electrons. The previous stored negative charge on the surface of cathodic barrier goes to nearly zero in the breakdown phase at $t_2 = 2.1$ μs and the successive growth of positive charge develops on the surface of cathodic barrier in the afterglow phase. The annihilation of cathode fall layer begins in the afterglow phase of discharge plasma at t_3 due to dense accumulation of ionic species, such as He^+, He_2^+ and N_2^+ on the surface of cathodic dielectric barrier. The charged particles are depleted through different kinetic interactions, such as dissociative recombination and charge transfer processes of different ionic species as mentioned in the tables 2.1 and 2.2. This increment in positive charge due to the deposition of ionic species on the surface of cathodic barrier is frozen at the end of current pulse at time (t_4).

6. Effect of relative permittivity or dielectric constant of dielectric barrier

The breakdown voltage of gas in DBD reactor can be either greatly enhanced or reduced by the impact of variable relative permittivity of the barrier, which helps in the formation of intense uniform glow and Townsend discharge modes. The spatial profiles of electrons density, strengths of axial and radial electric field are analyzed for the relative permittivity values of 2.5 and 10, which describe the characteristics of uniform Townsend and glow discharge modes as shown in figure 10.
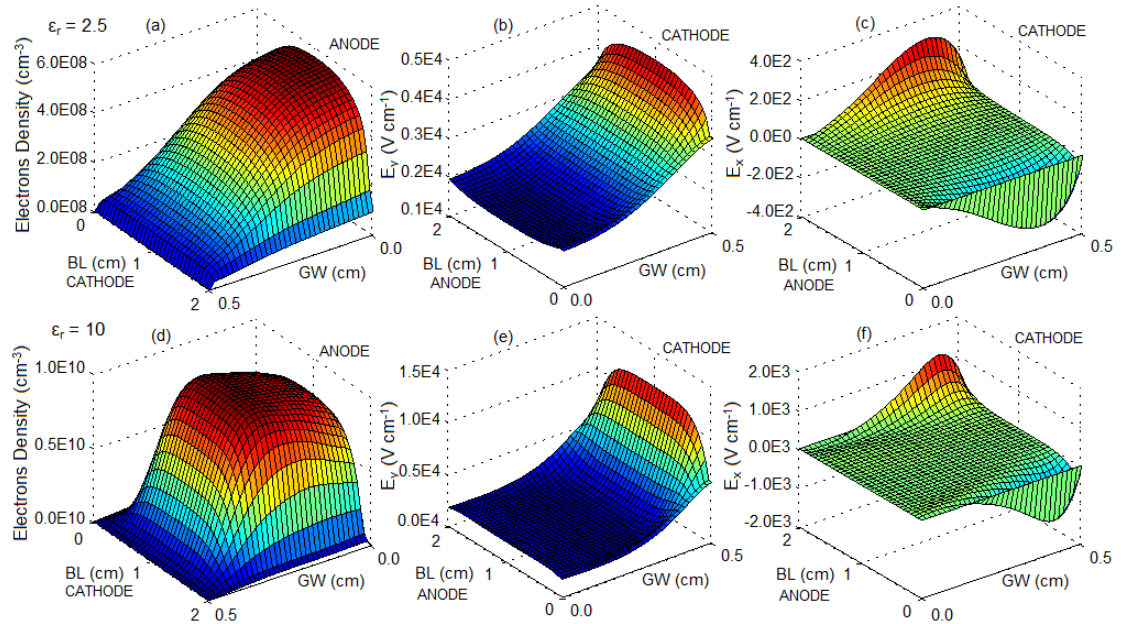

FIG. 10. Spatial distributions of electrons, strength of axial and radial electric field at distinct relative permittivity values $\varepsilon_r = 2.5$ and 10, for $f = 30$ kHz, Barrier width = 0.1 cm and $V_{appl} = 1.45$ kV with 20 ppm N_2 impurities.

The relative permittivity of dielectric barriers modifies the characteristics of atmospheric pressure discharge modes. However, the electrical behaviour of atmospheric pressure discharge plasma is described by the influence of relative permittivity, which exhibits the sharp fall of gas gap voltage with an increase in

relative permittivity of barrier [31] during the glow discharge mode at atmospheric pressure in pure helium gas. At small values of relative permittivity or dielectric constant, such as $\varepsilon_r = 2.5$, the breakdown is not strong, and ultimately the weak avalanche is formed due to the drop of small fraction of external applied potential across the gap. As a result, the Townsend mode of APD is possible, in which the peak of electron density is near the anodic barrier. The cathode fall region is expanded in the reactor gap and the axial electric field linearly varies from cathode towards anode barrier without any intense distortion near the cathode barrier, while the change in radial electric field is also expanded gradually in the reactor gap as well as on the surface of cathodic barrier as shown in figure 10 (a, b, c). The four distinct regions of a uniform glow discharge plasma are completely suppressed in case of Townsend discharge plasma. The spatial profiles of electrons density and axial electric field confirm that the atmospheric pressure Townsend discharge mode is formed at $\varepsilon_r = 2.5$ due to large impedance of dielectric barrier at lower dielectric constant as compared to higher dielectric constants. The discharge characteristics are modified at higher values of dielectric constant due to the reduction in the dielectric impedance, which favours in the formation of strong gas breakdown. This causes a higher fraction of the external imposed voltage to be dropped across the discharge gap, which results in a sudden rise in the discharge current pulse and the formation of a uniform glow discharge plasma. The profiles of electron density, axial and radial electric fields are completely changed under these conditions, and the result is a higher electron density in the negative glow region and the presence of strongly distorted electric field in the cathode fall layer. The radial electric field causes an extension of ionization on the surface of cathodic dielectric barrier in the radial direction in case of uniform glow discharge plasma as exhibited in figure 10 (d, e, f). The strength of radial electric field in the cathode fall region is used for the stabilization of uniform glow discharge plasma. The change in numerical values of discharge parameters are explained in table 3 for the uniform Townsend and glow discharge plasma modes.

Table 3

Dielectric constant (ε_r)	Electron density (cm^{-3})	Axial electric field (V cm^{-1})	Radial electric field (V cm^{-1})
2.5	5.0×10^{08}	4.0×10^{3}	$\pm5.0\times10^{2}$
10	1.0×10^{10}	1.2×10^{4}	$\pm2.0\times10^{3}$

It is evident from table 3 that the values electron density, axial and radial electric fields are sharply increased when the atmospheric pressure discharge is shifted from the uniform Townsend (dark) to glow discharge mode at different dielectric constants due to the significant effect of relative permittivity of dielectric barriers.

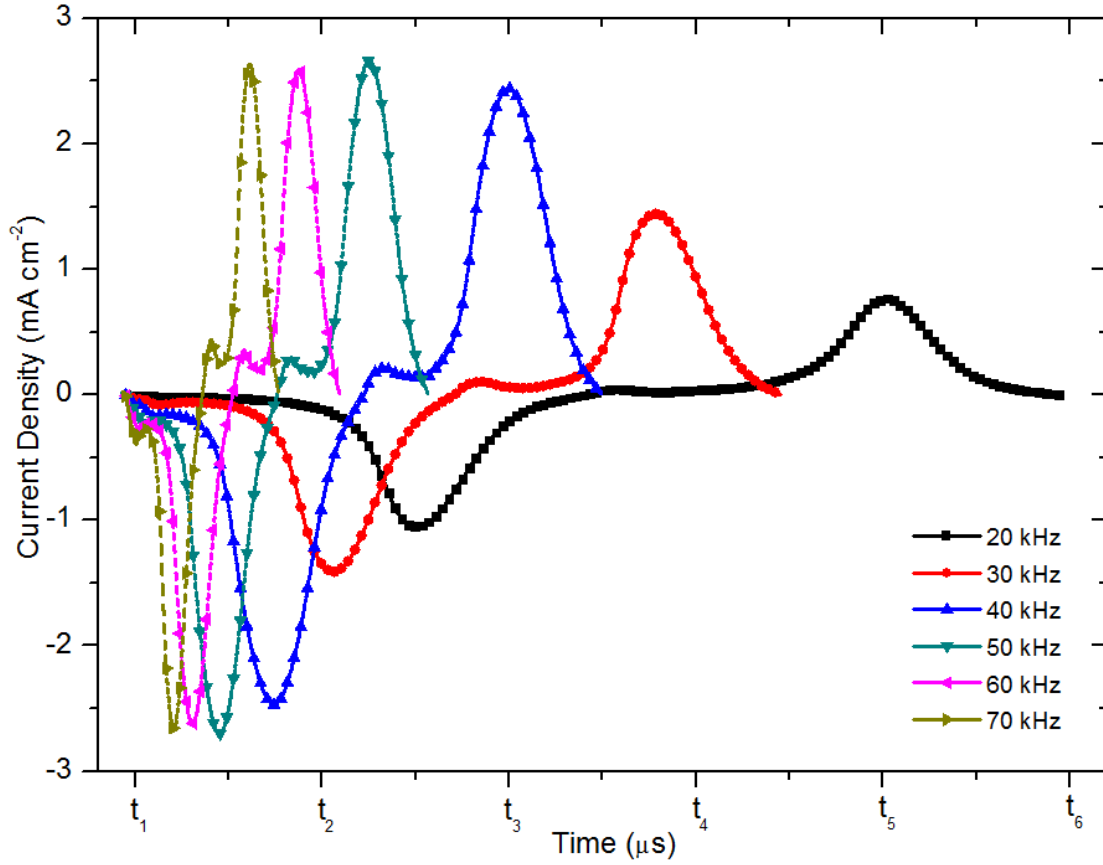## 7. Effect of driving frequencies

FIG. 11. Temporal evolution of conduction discharge current density for f = 20 - 70 kHz and V_{appl} = 1.45 kV with 20 ppm N_2 impurities.

To diagnose an effect of source driving frequency, the temporal analysis of conduction discharge current density is performed with a smaller magnitude of overvoltage for the dielectric barrier discharges. The stationary temporal profiles of current-voltage structure of uniform discharge plasma are identified in the indicated frequency domain as shown in figure 11, while the time scale (t_1 to t_6) along the horizontal direction represents the variable time periods for these frequencies. The marked amplification in the magnitude of current density is enhanced from 20 to 50 kHz in the alternate cycles, which becomes steady after 50 kHz. This increase in current density can be explained by the effect of electron energy losses and heating loss of ionic species in frequency domain. It has been described in literature that the increase in current is due to the transformation of electrical energies into kinetic energies, when the source driving frequency shifts from small to large values [32 - 34]. The electrons and ions in the positive move towards their momentary anodic and cathodic barrier depending on the polarity of imposed electric field. The displacement of ionic species is significantly greater across the reactor gap at lower frequencies than higher frequencies due to longer time period of a cycle. The coupling of input electrical energy becomes greater at higher frequencies than lower frequencies because the unconsumed charges on the surface of dielectric barrier from the previous discharge current pulse are strongly employed to extract electrical energies from the source potential. At small frequencies (< 20 kHz) in DBD, the primary portion of electrical energies is dissipated in the heating of excited and ionic species due to longer time period of a cycle, whereas this kind of dissipation loss becomes significantly small at higher frequencies. The conduction discharge current density is progressive from 20 to 50 kHz by the slump in electron energy losses. So, the

electrical energy linked with DBD is smoothly transformed into electron kinetic energies at higher frequencies than lower frequencies. This shows that the pre-ionization rate is increased with a rise in frequency due to the trapping of greater number of charged particles in the positive column, which results a higher current density at higher frequencies. The increase in the conduction current density ceases at higher frequencies (> 50 kHz) and the characteristics of uniform discharge plasma becomes independent of source driving frequency. In this higher frequency regime, the internal kinetic behaviour of charged particles is modified and the direction of drift motion of majority of charged particles is inverted before reaching the dielectric barriers of opposite polarity. This increases the production rate of charged particles due to the collisions with gas particles in the reactor gap. As a result, the source of secondary emission of electrons is reduced because the ionic species retrogress before striking the surface of cathodic barrier. So the source of fast accelerated electrons from the cathode fall is less at higher frequencies and ultimately caps further increment in the source of ionization. Another property of DBD plasma is that the residual current density is continuously raised from 20 to 70 kHz, which also supports the above arguments of strong trapping of the charged particles in the positive column. This analysis confirms that the characteristics of dielectric barrier discharges demand further spatial analysis of charged carriers in detail and will be discussed in the future simulation work with three dimensional self-consistent fluid model.

8. Conclusions

We present a self-consistent two-dimensional fluid modelling technique using the local mean energy approximation for pure helium and He-N_2 gases with variable amount of nitrogen impurities (20 and 50 ppm) including all important chemical reactions. The physical understanding of non-equilibrium uniform glow discharge plasma is advanced by the identification of a threshold criterion in pure helium and He-N_2 gases. A comparative analysis of gas breakdown potential for uniform and filamentary discharge plasma is performed by investigating the effect of magnitude of overvoltage in He-N_2 gas. The origin of non-uniformities (filaments) is distinguished in the breakdown and decay phases by the systematic variation of operating conditions. Filamentary discharges transform into uniform glow discharges when the driving frequency is increased over the range (5 → 25 kHz), which shows the creation and coalescence of filaments in the breakdown phase. The behaviour of electrons is illustrated by the spatial analysis of filamentary and uniform discharge plasmas in the breakdown phase. The properties of dielectric barrier material are examined by the effect of relative permittivity for the uniform Townsend and glow discharge modes. Finally, the dynamic progression in conduction discharge current density from (20 → 50 kHz) indicates that the coupling of electrical energy with DBD is unevenly transformed into electron kinetic energies of discharge plasma at different frequencies. Overall, this study is useful to deliver a satisfactory knowledge for the internal spatial behaviour of uniform and filamentary atmospheric pressure discharges, and to unfold the origin of non-uniformities under the range of operating conditions.

9. Acknowledgement

10. References

[1] Y. P. Raizer, Gas Discharge Physics, Springer-Verlag Berlin, 1991.

[2] S. Kanazawa, M. Kogoma, T. Moriwaki and S. Okazaki, J. Phys. D: Appl. Phys., Vol. 21, 838 - 840, 1988.

[3] T. Yokoyama, M. Kogoma S. Kanazawa, T. Moriwaki and S. Okazaki, J. Phys. D: Appl. Phys., Vol. 23, 374 -377, 1990.

[4] B. Eliasson and U. Kogelschatz, IEEE Transactions on Plasma Science, Vol. 19, 1063 - 1077, 1991.

[5] U. Kogelschartz, B. Eliasson and W. Egli, Pure Appl. Chem., Vol. 71, 1819 - 1828, 1999.

[6] U. Kogelschartz, IEEE Transactions on Plasma Science, Vol. 30, 1400 - 1408, 2002.

[7] M. Laroussi, G. E. Sayler, B. B. Glascock, B. Mccurdy, M. E. Pearce, N. G. Bright and C. M. Malott, IEEE Transactions on Plasma Science, Vol. 27, No. 1, 34-35, February 1999.

[8] K. H. Becker, U. Kogelschatz, K. H. Schoenbach R. J., Non-Equilibrium Air Plasmas at Atmospheric Pressure, (Series in Plasma Physics), 2004-11-29, Taylor & Franci.

[9] F. Massines, A. Rabehi, Ph. Decomps, R. B. Gadri, P. Segur and C. Mayoux, J. Appl. Phys., Vol. 83, 2950, 1998.

[10] L. Mangolini, C. Anderson, J. Heberlein and U. Kortshagan, J. Phys. D: Appl. Phys., Vol. 37, 1021 - 1030, 2004.

[11] Yu. B. Golubovsskii, V. A. Mairov, J. Behnke and J. F. Behnke, J. Phys. D: Appl. Phys., Vol. 36, 39 - 49, 2003.

[12] D. Braun, V. Gibalov and G. Pietsch, Plasma Sources Science and Technology, Vol. 1, 166 - 174, 1992.

[13] P. Zhang and U. Kortshagan, J. Phys. D: Appl. Phys., Vol. 39, 153 - 163, 2006.

[14] L. L. Alves, G. Gousset and C. Ferreira, Phys. Rev. E 55 (1), 890, 1997.

[15] G. J. M. Hagelaar, F. J. Hoog and G. M. W. Kroesen, Phys. Rev. E 62 (1), 1452, 2000.

[16] BOLSIG+, freeware, www.siglo-kinema.com/bolsig.htm.

[17] R. Deloche, P. Monchicourt, M. Cheret and F. Lambert, Phys. Rev., Vol. 13, No. 3, 1140 - 76, March 1976.

[18] C. B. Collins, H. S. Hicks, W. E. Wells and R. Burton, Phys. Rev. A 6, 1545, 1972.

[19] J. Stevefelt, J. M. Pouvesle and A. Bouchoule, J. Chem. Phys., Vol. 76, 4006, 1982.

[20] S. Rauf and M. J. Kushner, J. Appl. Phys., Vol. 85, 3460 - 3469, 1999.

[21] Pouvesle J. M., Bouchoule A. and Stevefelt J., J. Chem. Phys., Vol. 77, 817 - 825, 1982.

[22] X. Yuan and L. L. Raja, IEEE Transactions on Plasma Science, Vol. 31, No: 4, August 2003.

[23] Brunger M., Buckman S. J. and Allen L. J., J. Phys. B: At. Mol. Opt. Phys. 25 1823 - 38, 1992.

[24] G. J. M. Hagelaar, PhD Thesis, Technische Universiteit Eindhoven, 2000.

[25] Scharfetter D. L. and Gummel H. K., IEEE Transactions on Electron Devices, Vol. 16, 64 - 77, 1969.

[26] Anderson C., Hur M. and Zhang P, J. Appl. Phys., Vol. 96, 1835 - 1839, 2004.

[27] T. Shirafuji, T, Kitagawa, T. Wakai and K. Tachibana, Appl. Phys. Lett., Vol. 83, No. 12, 22nd September 2003.

[28] L. Candido, Jose-Pedro Rinoy, N. Studarty and F. M. Peeters, J. Phys. Condens. Matter, 10 (1998) 11627–11644.

[29] D. Lee, J. M. Park, A. H. Hong and Y. Kim, IEEE Transactions on Plasma Science, Vol. 33, No. 2, 949 - 957, 2005.

[30] F. Massines, P. Ségur, N. Gherardi, C. Khamphan and A. Ricard, Surface and Coatings Technology, Volumes 174-175, September-October 2003, Pages 8-14.

[31] F. Tochikubo, T. Chiba and T. Watanabe, Jpn. J. Appl. Phys., Vol. 38, 5244 - 5250, 1999.

[32] QU Qiong-Rong, Meng Zhao-Xing, Chin. Phys. Lett., Vol. 21, No.7, 1317, 2004.

[33] A. M. Howaton, Introduction to gas discharge, second edition, Pergamon press, Oxford.

[34] Xu Tao Deng and M. G. Kong, IEEE Transactions on Plasma Science, Vol. 32, No. 4, pp. 1709 - 1715, December 2004.